

Structural and optical properties of sulfur passivated epitaxial step-graded GaAs_{1-y}Sb_y materials

Mantu K. Hudait, Michael B. Clavel, Sarat Saluru, Jheng-Sin Liu, Michael A. Meeker, Giti A. Khodaparast, and Robert J. Bodnar

Citation: *AIP Advances* **8**, 115119 (2018); doi: 10.1063/1.5028133

View online: <https://doi.org/10.1063/1.5028133>

View Table of Contents: <http://aip.scitation.org/toc/adv/8/11>

Published by the [American Institute of Physics](#)



Don't let your writing
keep you from getting
published!

AIP | Author Services

Learn more today!

Structural and optical properties of sulfur passivated epitaxial step-graded GaAs_{1-y}Sb_y materials

Mantu K. Hudait,^{1,a} Michael B. Clavel,¹ Sarat Saluru,¹ Jheng-Sin Liu,¹

Michael A. Meeker,² Giti A. Khodaparast,² and Robert J. Bodnar³

¹Advanced Devices & Sustainable Energy Laboratory (ADSEL), Bradley Department of Electrical and Computer Engineering, Virginia Tech, Blacksburg, Virginia 24061, USA

²Department of Physics, Virginia Tech, Blacksburg, Virginia 24061, USA

³Fluids Research Laboratory, Department of Geosciences, Virginia Tech, Blacksburg, Virginia 24061, USA

(Received 7 March 2018; accepted 2 November 2018; published online 15 November 2018)

The impact of bulk and surface defect states on the vibrational and optical properties of step-graded epitaxial GaAs_{1-y}Sb_y ($0 \leq y \leq 1$) materials with and without chemical surface treatment by (NH₄)₂S was investigated. Tunable antimony (Sb) composition GaAs_{1-y}Sb_y epitaxial layers, grown by solid source molecular beam epitaxy (MBE), were realized on GaAs and Si substrates by varying key growth parameters (*e.g.*, Sb/Ga flux ratio, growth temperature). Raman and photoluminescence (PL) spectroscopic analysis of (NH₄)₂S-treated GaAs_{1-y}Sb_y epitaxial layers revealed composition-independent Raman spectral widths and enhanced PL intensity (1.3×) following (NH₄)₂S surface treatment, indicating bulk defect-minimal epitaxy and a reduction in the surface recombination velocity corresponding to reduced surface defect sites, respectively. Moreover, quantification of the luminescence recombination mechanisms across a range of measurement temperatures and excitation intensities (*i.e.*, varying laser power) indicate the presence of free-electron to neutral acceptor pair or Sb-defect-related recombination pathways, with detectable bulk defect recombination discernible only in binary GaSb PL spectra. In addition, PL analysis of the short- and long-term thermodynamic stability of sulfur-treated GaAs_{1-y}Sb_y/Al₂O₃ heterointerfaces revealed an absence of quantifiable atomic interdiffusion or native oxide formation. Leveraging the combined Raman and PL analysis herein, the quality of the heteroepitaxial step-graded epitaxial GaAs_{1-y}Sb_y materials can be optimized for optical devices. © 2018 Author(s). All article content, except where otherwise noted, is licensed under a Creative Commons Attribution (CC BY) license (<http://creativecommons.org/licenses/by/4.0/>). <https://doi.org/10.1063/1.5028133>

I. INTRODUCTION

Composition-dependent, mixed-anion GaAs_{1-y}Sb_y materials offer unique opportunities to design electronic and optoelectronic devices due to their smaller hole and electron effective masses, tunable optical bandgap, and tunable band offsets with In_xGa_{1-x}As.¹⁻¹⁰ In addition, its binary compounds (*i.e.*, GaAs, GaSb) serve as substrates for pseudomorphic or lattice mismatched metamorphic epitaxy. These material systems offer different types of band alignment configurations with other semiconductors, such as the type-I (straddling) band alignment between GaSb and AlSb, the type-II (staggered) band alignment between InAs and AlSb, and the type-III (broken) band alignment between InAs and GaSb.^{11,12} Furthermore, GaAsSb materials can be grown pseudomorphically on InP or GaSb substrates. Although a large-area 150 mm GaSb (InP) wafer is currently being developed, wafer costs continue to hinder the economy-of-scale production of GaAsSb-based devices. On the other hand, the mature technology of producing large-area, 150 mm - 200 mm GaAs wafers, and the epitaxy of

^aContact author: Tel: (540) 231-6663, Fax: (540) 231-3362, E-mail: mantu.hudait@vt.edu

device-quality GaAs_{1-y}Sb_y on GaAs and ultimately 300 mm Si wafers utilizing III-V metamorphic buffer architectures, will provide a feasible path for cost-effective GaAsSb-based electronic and optoelectronic devices. However, there are many challenges that arise in attempting to use GaAsSb-based materials for heterojunction tunnel field-effect transistors (TFETs),^{2,13-18} heterojunction bipolar transistors (HBTs),¹⁹⁻²² and optoelectronic devices,^{1,23-30} including: (i) the miscibility gap in GaAs_{1-y}Sb_y materials; (ii) difficulty in realizing mixed As-Sb epitaxy due to competing surface adatom mobilities and the effect of temperature, atomic flux ratio, and anion surface incorporation as a function of desired Sb composition; (iii) prohibitively high bulk defect densities when heterogeneously integrating GaAs_{1-y}Sb_y-based materials on lattice mismatched GaAs or Si substrates;³¹⁻³⁴ and (iv), the minimization, *via* chemical surface treatment or other means, of surface defect states resulting from group V dimerization (*e.g.*, Sb-Sb) or dangling bond formation.³⁵⁻⁴⁹

Previous attempts to resolve these challenges focused largely on single-step Sb composition-dependent GaAs_{1-y}Sb_y materials ($0.08 \leq \text{Sb} \leq 0.72$) grown on GaAs substrates by either molecular beam epitaxy (MBE) or organometallic-vapor phase epitaxy.^{3-5,7} On the other hand, Yano *et al.* utilized both single- and multi-step-graded buffer architectures to realize a GaAs_{0.45}Sb_{0.55} upper-most epilayer.³ In the case of a single-step buffer architecture, misfit dislocations (MDs) are confined to the epilayer/substrate interface, which can lead to 3-dimensional growth as a result of the large epilayer/substrate lattice mismatch and thereby increased strain energy at the growth front. Correspondingly, the defect density in such single-step buffer architectures is increased. Alternatively, step-graded buffer architectures allow for the incremental accommodation of epilayer/substrate lattice mismatch, thereby allowing for layer-by-layer growth to be preserved given steps of sufficiently low lattice mismatch. In turn, this minimizes defect propagation in the growth direction and, ultimately, within the overlying epitaxial layer of interest. As there is minimal work reporting the heterointegration of GaAs_{1-y}Sb_y materials on Si,³¹ either *via* the step-graded or single-step buffer approach, such investigations into the material synthesis and characterization of direct-epitaxy GaAs_{1-y}Sb_y materials on Si are mandated.

In order to address the above issues, *this work* describes (i) the synthesis of tunable Sb composition GaAs_{1-y}Sb_y ($0.15 \leq \text{Sb} \leq 0.62$) materials heterogeneously integrated on GaAs and Si substrates using a step-graded metamorphic buffer architecture; (ii) the composition- and thickness-dependent vibrational properties of GaAs_{1-y}Sb_y epitaxial layers and their correlation to bulk defect-related Raman spectroscopy features; (iii) the optical properties of GaAs_{1-y}Sb_y epitaxial layer and their comparison to binary GaAs and GaSb materials so as to quantify the presence, if any, of bulk defects in the as-grown mixed As-Sb materials; and (iv), the effect of (NH₄)₂S-based chemical surface treatments on the vibrational and optical properties of GaAs_{1-y}Sb_y epitaxial layers and GaAs_{1-y}Sb_y/Al₂O₃ heterointerfaces. Moreover, the short- and long-term thermodynamic stability of the (NH₄)₂S-treated GaAs_{1-y}Sb_y heterointerface was investigated utilizing photoluminescence spectroscopy (PL). The relationship between Sb composition and its spectroscopic signatures (*e.g.*, Raman frequency, PL wavelength) on the bulk and surface defects in epitaxial GaAs_{1-y}Sb_y materials, provide a pathway for the realization of mixed As-Sb-based optoelectronic devices.

II. EXPERIMENTAL

A. Materials synthesis

GaAs_{1-y}Sb_y epitaxial layers with tunable Sb composition were grown by solid source MBE on semi-insulating (100)/2° GaAs substrates, or in the case of the 55% Sb composition GaAsSb, on Si using step-graded metamorphic buffer architecture. Figure 1 shows the cross-sectional schematic of the step-graded GaAs_{1-y}Sb_y layer structures on GaAs and Si substrates, with tunable Sb composition, that were investigated in this work. The layer structure was grown *via* MBE on (100) GaAs substrates which were offcut 2° towards the <110> direction, as well as on (100)/6° offcut Si substrate with GaAs buffer. The off-cut Si substrate, combined with cyclical thermal annealing and a migration-enhanced epitaxy, two-step growth process (*i.e.*, low temperature and low growth rate; high temperature and high growth rate), were used for the formation of two-atomic layer steps on the Si surface, thereby minimizing the formation of anti-phase domains (APDs). The low temperature nucleation of GaAs

GaAs _{0.79} Sb _{0.21} 500 nm	GaAs _{0.54} Sb _{0.46} 500 nm	GaAs _{0.36} Sb _{0.62} 500 nm	GaAs _{0.46} Sb _{0.56} 500 nm
GaAs _{0.81} Sb _{0.19} 500 nm	GaAs _{0.56} Sb _{0.42} 500 nm	GaAs _{0.41} Sb _{0.59} 500 nm	GaAs _{0.59} Sb _{0.41} 500 nm
GaAs _{0.85} Sb _{0.15} 500 nm	GaAs _{0.54} Sb _{0.36} 500 nm	GaAs _{0.56} Sb _{0.44} 500 nm	GaAs _{0.72} Sb _{0.28} 500 nm
GaAs 500 nm	GaAs 500 nm	GaAs 500 nm	GaAs 2 μm
(100)2° GaAs	(100)2° GaAs	(100)2° GaAs	(100)6° Si
(a) Sample-A	(b) Sample-D	(c) Sample-H	(d) Sample-F

FIG. 1. Schematic of Sb composition dependent GaAs_{1-y}Sb_y layers grown on (a)-(c) GaAs and (d) Si substrate, respectively. GaAsSb epitaxial layers were grown at a constant temperature of 440°C on Si substrate and 410°C-450°C on GaAs substrate to modulate the Sb composition in GaAsSb layer. The lower growth temperature was for the higher Sb composition sample.

on Si (~400°C and 0.1 μm/hr) is a critical step in avoiding the formation of APDs. Subsequent GaAs epitaxy at 600°C, followed by thermal cycle annealing, was utilized to reduce the defects due to the 4% lattice mismatch between the Si substrate and the GaAs layer, and was immediately followed by the deposition of the step-graded GaAs_{1-y}Sb_y epitaxial layers. Table I shows the detailed sample structure and analysis methods used in this work. The Sb flux was provided by a low temperature, 125cc Sb effusion cell and arsenic valved cracker source for As₂ flux with the cracking zone held at 900°C. Substrate oxide desorption was performed at ~735°C under a constant As₂ flux and the surface was monitored by *in-situ* reflected high energy electron diffraction. A 0.5 μm/hr growth rate (*i.e.*, gallium rate) was used for all GaAsSb epitaxial layers. A fixed As₂/Ga ratio of 10 and Sb/Ga ratio in the range of 1 to 6 to modulate Sb composition were used for GaAs_{1-y}Sb_y growth on Si at 440°C substrate temperature. The growth temperature on the GaAs substrate ranged from 410 to 450°C to control the Sb composition in the GaAs_{1-y}Sb_y layer. In order to achieve the higher Sb composition, a higher Sb/Ga ratio and lower growth temperature were used during growth. In addition, to accommodate the lattice mismatch between the top GaAs_{1-y}Sb_y layer of interest and the GaAs substrate as well as to reduce the threading dislocation density in the final GaAs_{1-y}Sb_y layer, a two step-graded GaAsSb layer with different Sb compositions was incorporated in each run. The thickness of each step in the step-graded buffer was set approximately to 500 nm. Additionally, select GaAsSb epitaxial layers were degreased using acetone, isopropanol, and deionized (DI) water. After degreasing, the samples were dipped into 20% (NH₄)₂S aqueous solutions for 3 to 10 minutes durations. 4 nm and 10 nm (1.06 Å/cycle) Al₂O₃ oxides were then deposited in order to evaluate the interface properties. The oxide depositions were performed at 250°C using a Cambridge NanoTech ALD system with trimethylaluminum (TMA) and DI water as precursors. The growth parameters

TABLE I. Summary of GaAsSb layer structures studied in this work. The substrate used for GaAsSb layer, number of steps in graded buffer architecture, final Sb composition in the uppermost GaAsSb layer, Raman and Photoluminescence measurement on selected samples.

Sample identity (substrate)	Buffer layer	Total number of GaAsSb steps	Final Sb composition	Raman analysis	PL analysis
GaAs substrate				Y	Y
A (GaAs)		3	21	Y	
B (GaAs)		3	34	Y	Y
C (GaAs)		3	44	Y	Y
D (GaAs)		3	46	Y	
E (GaAs)		4	51	Y	
F (Si)	2.0 μm GaAs	3	55	Y	Y
G (GaAs)		3	57	Y	
H (GaAs)		3	62	Y	Y
B (GaAs)		3	34		With Al ₂ O ₃
GaSb epi-layer				Y	
GaSb substrate				Y	Y

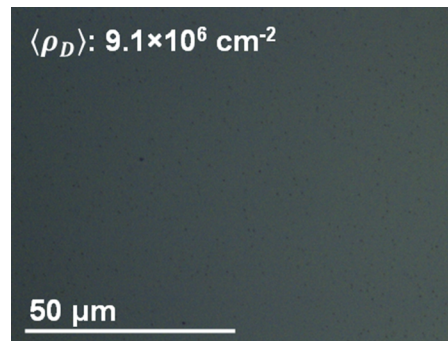


FIG. 2. Etch pitch density as determined on the surface of the GaAs_{1-y}Sb_y/GaAs/Si structure using a dilute HCl:H₂O₂:H₂O (2:1:80 volume ratio) etchant. The average defect density, $\langle \rho_D \rangle$, was found to be $\sim 9 \times 10^6 \text{ cm}^{-2}$ in the upper-most GaAs_{0.45}Sb_{0.55} epilayer.

used for the different GaAs_{1-y}Sb_y layers and the detailed x-ray analysis for the determination of Sb composition in each layer were reported earlier.^{31,49}

B. Materials characterization

The Sb alloy composition and strain relaxation properties of GaAs_{1-y}Sb_y layer were characterized using a Panalytical X'pert Pro system with CuK α -1 as the x-ray source. Micro-Raman spectroscopy was used to determine the vibrational properties from the surface and Sb composition/depth-dependent GaAsSb materials, having an estimated penetration depth of approximately 20-30 nm using a JY Horiba LabRam HR800 system equipped with a 514.32 nm Ar laser excitation source. The thickness of each step in the step-graded buffer, the interface quality between atomic layer deposited Al₂O₃ and GaAsSb, and the defect properties of the GaAs_{1-y}Sb_y epilayers were examined using high-resolution transmission electron microscopy (TEM) analysis performed using a JEOL 2100 microscope. The electron-transparent foils of thin-film cross-section of GaAs_{1-y}Sb_y/GaAs/Si were prepared using standard mechanical polishing techniques followed by dimpling and low-temperature Ar⁺ ion milling. Additionally, in order to quantify the defect density in the upper-most GaAs_{0.45}Sb_{0.55} epilayer, etch pitch density (EPD) analysis was performed using a dilute HCl:H₂O₂:H₂O (2:1:80 volume ratio) etchant. Prior to etching, each sample was degreased using a standard acetone/isopropyl alcohol/de-ionized water sequence for 2 min, followed by native oxide removal in dilute NH₄OH:H₂O (1:15 volume ratio) for 30 s. The selection of oxide etchant and dilution were chosen so as to avoid deleterious surface roughening and prevent unwanted GaAs_{0.45}Sb_{0.55} etching. The samples were then immediately introduced into the dilute HCl-based etchant for 8 s. Figure 2 shows a representative optical micrograph taken of the surface of the GaAs_{0.45}Sb_{0.55}/GaAs_{1-y}Sb_y/GaAs/Si structure, wherein each black dot represents a singular defect (etch pitch), noting that the average defect density was found to be $\sim 9 \times 10^6 \text{ cm}^{-2}$. Lastly, photoluminescence experiments were performed using a Ti:Sapphire laser with a repetition rate of 80 MHz and a pulse duration of ~ 140 fs. The excitation wavelength was 700 nm, with a spot size of ~ 200 μm . The light was sent through a 0.55 m focal length spectrometer and collected by an enhanced InGaAs detector, using a standard lock-in detection scheme with a chopper frequency of ~ 331 Hz and temperature ranging from 77 K to room temperature.

III. RESULTS AND DISCUSSION

A. Sb composition profile via SIMS measurement

Figure 3 shows the SIMS profile of the 3-step GaAsSb layer on Si (Sample-F). The Sb composition of each layer is included in this figure. A 30 nm Al₂O₃ oxide layer was deposited by ALD prior to the SIMS measurement for the protection of the upper-most GaAs_{0.45}Sb_{0.55} layer. One can find from Figure 3 that the Ga concentration is constant throughout the layer structure since the Ga

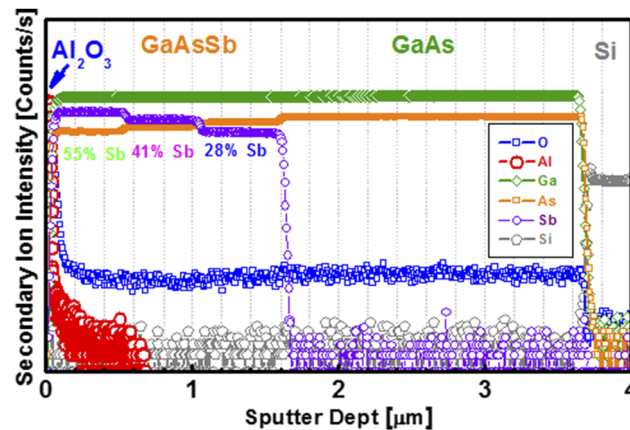


FIG. 3. SIMS profile of three step $\text{GaAs}_{1-y}\text{Sb}_y$ layers (55% Sb, 41% Sb, 28% Sb) grown on Si substrate using GaAs buffer layer. The 30 nm ALD Al_2O_3 was deposited on the upper-most GaAsSb layer prior to SIMS measurement. The Ga concentration is constant since the growth rate was fixed during growth and the Sb concentration was modulated by varying Sb/Ga ratios.

flux (*i.e.*, growth rate) was kept constant during the growth of this structure. The Sb/Ga ratio was varied during growth to achieve tunable Sb compositions, ranging from 28% to 55%. The step-graded GaAsSb layer, as shown in Figure 3, was created by varying the As and Sb fluxes at a constant growth temperature of 440°C on Si. Moreover, sharp heterointerfaces between each $\text{GaAs}_{1-y}\text{Sb}_y$ layer are observed, and the oxygen level within the GaAsSb layer structure as well as within GaAs buffer layer are almost identical. This implies that there was no additional oxygen provided by the Sb source during the growth of step-graded $\text{GaAs}_{1-y}\text{Sb}_y$ epitaxial layer.

B. Sb composition dependent vibrational properties via Raman spectroscopy

Raman spectroscopy was used in order to determine the longitudinal optical (LO) and transverse optical (TO) phonon frequencies of the prepared GaAsSb samples, allowing for the determination of the Sb composition. Figure 4(a) shows the Raman frequency shift as a function of Sb composition in $\text{GaAs}_{1-y}\text{Sb}_y$ layers studied in this work. Each reported Sb composition was grown using step-graded $\text{GaAs}_{1-y}\text{Sb}_y$ metamorphic buffers on GaAs substrates. As shown, both the LO and TO phonon frequencies shift toward lower wavenumber as the Sb concentration increases. Also, the Raman signals from the surface of epitaxial GaSb and GaSb substrates both show a peak located at 234 cm^{-1} (TO phonon frequency), indicating the superior quality of the GaSb epitaxial layer growth. The quality of the GaSb epitaxial layer would be inferior if the peak position from the GaSb epitaxial layer is shifted towards higher wavenumbers (due to the incorporation of residual arsenic from the MBE chamber) or if the full width at half maximum (FWHM) of the GaSb epilayer is higher than the GaSb substrate (due to defective or poor quality epitaxial layer growth). In Figure 4(a), each spectrum was normalized and shifted vertically, and the peak fitting was performed using Lorentzian-shaped spectra to identify the GaAs-like LO/TO and GaSb-like LO/TO phonon peaks. Figure 4(b) shows the relationship between the Raman frequency shift and the Sb concentration in $\text{GaAs}_{1-y}\text{Sb}_y$. The Raman peaks in the range 200 cm^{-1} - 300 cm^{-1} are most relevant for determining the Sb composition dependence of GaAsSb samples. The LO phonon peak is the dominant Raman peak, with the less intense TO phonon peak occurring below 240 cm^{-1} . The Raman spectra of the GaSb epilayer and the Te-doped *n*-type GaSb substrate are nearly identical, with both the LO and TO phonon peaks clearly evident in Figure 4(a). It is interesting to note that these phonon peaks (234 cm^{-1} for the LO, and 225 cm^{-1} for the TO) are slightly different than those reported in the literature (GaSb-related LO phonon peak at 237 cm^{-1} and TO phonon peak at 230 cm^{-1}).^{4,6,7} This shift is attributed to the quality of the GaAsSb materials produced during the growth process in this study, whereas tunable Sb composition GaAsSb materials were produced by a single-step buffer on GaAs or InP substrate by other researchers.^{4,6,7} The phonon peak separation is associated with the residual strain present in the GaAsSb layer because the Raman frequency shift is sensitive to the local strain environment

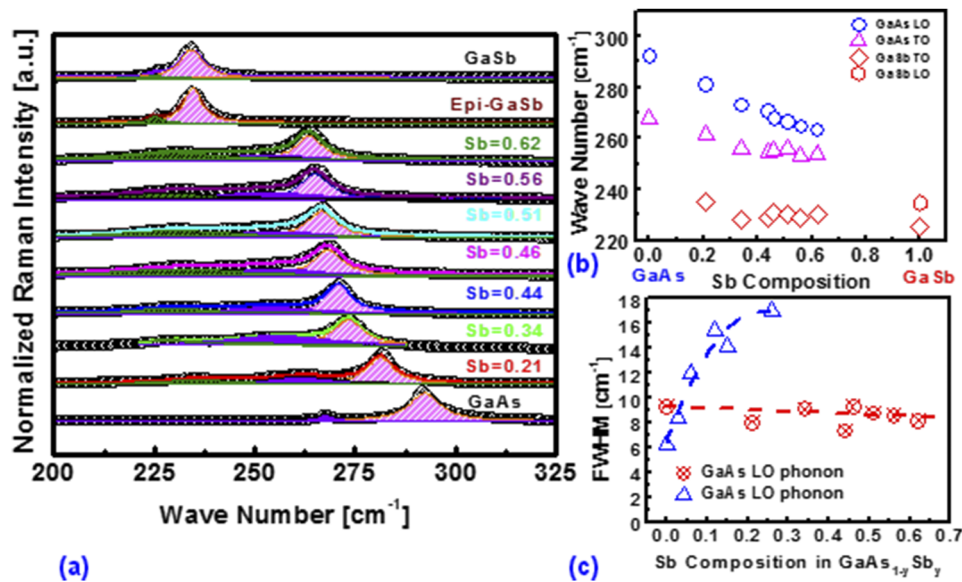


FIG. 4. (a) Room temperature Raman spectra from the surface of GaAs_{1-y}Sb_y layer (without sulfur passivation) as a function of Sb composition. (b) Relationship between the Raman frequency shift and the Sb composition in GaAs_{1-y}Sb_y. (c) FWHM of LO phonon peak as a function of Sb composition. The data point shown by triangles in 4c are taken from Ref. 50. As shown in figure (a) and (b), both LO and TO phonon frequencies were shifted towards lower wavenumber as Sb alloy composition increases in GaAsSb, as expected. In addition, the lower FWHM compared with literature indicates superior quality GaAs_{1-y}Sb_y material.

present in the film. This can be further supported by the FWHM of the GaAs-related LO phonon peak as a function of Sb composition, noting that the FWHM of GaAs LO phonon peak is almost constant with increasing Sb content, which was attributed to the mitigation of dislocations by using a step-graded buffer. Unless defects are confined within the step-graded buffer, the FWHM of the uppermost GaAsSb layer will increase with Sb composition. In addition, the GaAs-like LO and TO phonon mode frequency shift decreases with increase in Sb composition, however, there is no significant variation of the GaSb-related phonon peaks. One can find from Figure 4(c) that the FWHM of the GaAs LO phonon peak is nearly constant as a function of Sb composition up to the maximum amount (62%) studied in this work. The FWHM of GaAsSb nanowires grown on GaAs substrates as a function of Sb compositions from Kasanaboina *et al.*⁵⁰ is also included in Figure 4(c). In these samples, the FWHM of the GaAsSb layer increases with increasing Sb composition, which is due to the composition inhomogeneity and dislocations presents inside the GaAsSb layer. On the other hand, the FWHM is almost constant as a function of Sb composition in this work, wherein higher Sb composition implies higher lattice mismatch with respect to the GaAs substrate, thus indicative of the superior quality GaAsSb epitaxial layers achieved solely via the intermediate buffer architecture. Consequently, one must account for the buffer architecture between the GaAsSb epilayer of interest and the substrate in order to mitigate the defect and dislocation propagation into the active material(s). This can be further supported by cross-sectional TEM microscopy, where one can expect a minimal density of defects within the uppermost GaAsSb layer.

C. Depth dependent vibrational properties via Raman spectroscopy

Raman spectroscopy was used to determine the phonon peak position in step-graded buffer layers at various locations after selectively wet etching the GaAs_{1-y}Sb_y film, which was grown on Si, as shown in Figure 3. Figure 5(a) shows the cross-sectional TEM photomicrograph of the GaAs_{0.45}Sb_{0.55} layer grown on the Si substrate (Sample-F) using three intermediate step-graded GaAs_{1-y}Sb_y layers and a GaAs buffer layer. As shown in this figure, the defects are well confined within the GaAs layer and each step-graded GaAsSb buffer layer shows increasingly fewer defects. The sample was wet etched and the labels T₁-T₄ are the locations in the sample where Raman measurements were

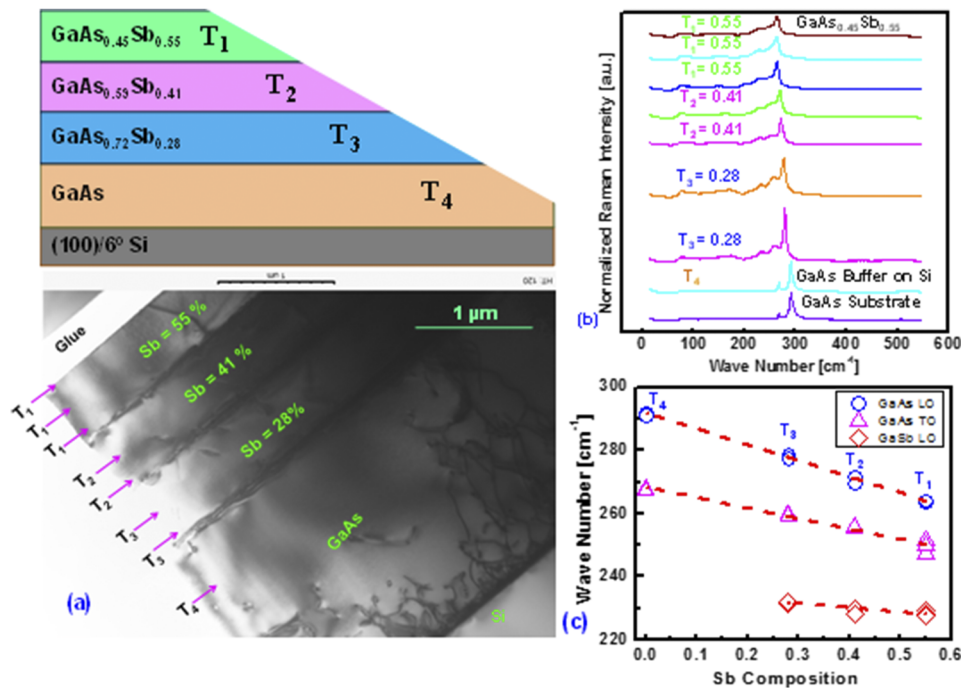


FIG. 5. (a) Cross-sectional TEM photomicrograph of the 3-step $\text{GaAs}_{1-y}\text{Sb}_y$ layer grown on Si using GaAs buffer layer (Sample-F). Labels T_1 - T_4 represent the locations on the sample where Raman analyses were performed to observe the evolution of the Raman peak as a function of Sb composition and the interface effect. (b) Room temperature Raman spectra from locations T_1 - T_4 and from the GaAs substrate. (c) Relationship between the Raman frequency shift and the Sb composition in $\text{GaAs}_{0.45}\text{Sb}_{0.55}$ sample as a function of etched locations T_1 - T_4 . Figures (b) and (c) suggest the abrupt change in Sb composition from one layer to the next layer and absence of Sb composition gradient at the interface.

performed. Figure 5(b) shows the room temperature Raman spectra as a function of wavenumber from the different locations in the sample, as labelled in Figure 5(a). The layer composition was further identified from the relationship between the wavenumber and the Sb composition as well as by x-ray analysis. Figure 5(c) shows the wavenumber versus Sb composition for the different locations (T_1 - T_4) in the sample. Raman peaks shift toward the GaAs side with decreasing GaAsSb layer thickness. Another interesting feature is that the peak position at T_3 (different part of the film shown in Figure 5(a)) is almost identical for different thicknesses, suggesting a uniform Sb composition and abrupt interfaces. There is no gradual change in composition in the film or change in composition at the interface, supported by the results shown in Figure 5(b). The Sb composition determined from the peak position shown in Figure 5(b) as a function of distance from the heterointerface agrees reasonably well with the results presented in Figure 4(b). This agreement indicates that there is an abrupt change in composition from one layer to the next and no composition gradient exists at the interface - this was achieved by selection of the proper growth temperature and group-V fluxes, as discussed above. Moreover, the Raman peak position from the surface of a bulk GaAs substrate is identical to that from the GaAs buffer layer on Si, irrespective of the 4% lattice mismatch, indicating a minimal defect density present within the GaAs buffer layer when grown on Si. If this were not the case, then one would expect a higher FWHM from the GaAs buffer layer as compared to the GaAs substrate. This is the first experimental demonstration of depth-dependent Raman measurement following growth of a step-graded buffer and its correlation with the bulk material. Thus, depth-dependent Raman analysis is a potential method to determine the composition shift should any ternary-composition materials form during GaAsSb materials synthesis.

D. Effect of sulfur passivation on optical properties via PL spectroscopy

GaAsSb mixed-anion materials are important for several device applications, but native complex oxides⁴⁰ often form on the surface and their removal by wet chemical processes hinders the electrical

and optical properties. It has been reported that As-O bonding and anti-bonding are located in the bandgap⁵¹ and elemental Sb on the surface produces a conductive path which can lead to high surface leakage current.^{35–37,51} Recently, we have demonstrated that processes using either $(\text{NH}_4)_2\text{S}$ or the combination of HCl and $(\text{NH}_4)_2\text{S}$ on GaAsSb materials were essential for removing the native oxides and passivating the surface dangling bonds.³⁹ Moreover, we have employed x-ray photoelectron spectroscopy (XPS) to determine the change in chemical state progression as a function of surface pre-clean and passivation, as well as energy band alignment parameters of the atomic layer deposited Al_2O_3 on tunable $\text{GaAs}_{1-y}\text{Sb}_y$ materials.³⁹ Removal of native oxides such as, Sb_2O_3 , Ga_2O_3 , and As_2O_3 by wet chemical etching and sulfur passivation will decrease surface states and reduce the surface recombination velocity, which in turn results in higher photoluminescence intensity. Figure 6 shows the PL intensity from the surface of a $\text{GaAs}_{0.56}\text{Sb}_{0.44}$ sample (Sample-C) as a function of $(\text{NH}_4)_2\text{S}$ passivation time. The surface was pre-cleaned with HCl prior to $(\text{NH}_4)_2\text{S}$ passivation because HCl will effectively remove the surface native oxides^{39,52} and $(\text{NH}_4)_2\text{S}$ will successfully passivate the surface. If the surface dangling bonds were passivated by sulfur, thus decreasing the surface states, then the PL intensity *must* increase with the effect of surface passivation. One can find from Figure 6 that the PL peak intensity increased after 10 min of surface passivation under 20% $(\text{NH}_4)_2\text{S}$ as compared with the unpassivated surface. The sulfur passivation was effective at 10 min, successfully removing the unwanted native oxides^{39,52} and passivating the surface dangling bonds. The PL peak position at 0.85 eV is almost constant with passivation time, indicating the Sb composition inside the uppermost $\text{GaAs}_{0.56}\text{Sb}_{0.44}$ layer was not affected by the passivation. If there was a deficiency (or loss) of Sb from the uppermost layer of $\text{GaAs}_{0.56}\text{Sb}_{0.44}$ film due to the formation of native oxide, the PL peak position would be shifted to higher bandgap due to lower Sb composition in the GaAsSb film.

Once the $\text{GaAs}_{0.56}\text{Sb}_{0.44}$ surface was successfully passivated, temperature and laser power dependent PL measurements were performed. The different recombination processes are strongly dependent on the quality of the materials and the measurement conditions, such as laser power and measurement temperature. For example, at lower temperature, recombination due to bound excitons and donor-acceptor pairs (DAP) are generally observed, and the total PL intensity is increased at low temperature as compared to room temperature. Moreover, an increase in temperature leads to a red shift in the PL peak position, which is attributed to electron-phonon interactions and lattice expansion at higher temperature.⁵³ In addition, the power dependence of the PL spectra would enable one to distinguish between, for example, free-to-bound (*i.e.*, free-electrons to acceptors), donor-to-acceptor pair (DAP) or Sb-defects-related recombination. Figure 7(a)–(e) shows the temperature and power dependent PL spectra of the $\text{GaAs}_{0.56}\text{Sb}_{0.44}$ sample (Sample-C), after 10 min surface passivation in $(\text{NH}_4)_2\text{S}$ solution. As discussed above, the sample was pre-cleaned with HCl prior to sulfur passivation. The PL spectra are asymmetric, and there is a high energy Gaussian tail and a sharp cut-off at the low energy side, indicating the high purity of the GaAsSb material. In a direct bandgap semiconductor,

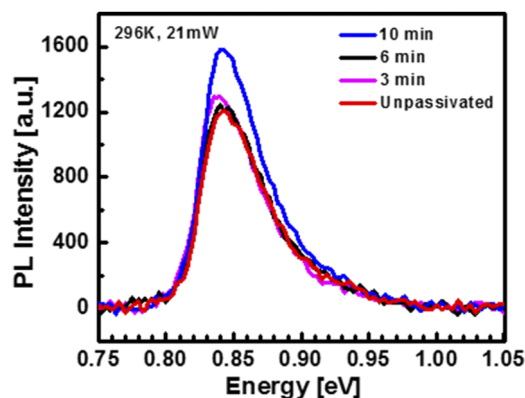


FIG. 6. PL intensity of $\text{GaAs}_{0.56}\text{Sb}_{0.44}$ sample (Sample-C) as a function of $(\text{NH}_4)_2\text{S}$ passivation time. The surface was pre-cleaned with HCl prior to $(\text{NH}_4)_2\text{S}$ passivation. The 1.3× enhancement of PL intensity compared with unpassivated surface of $\text{GaAs}_{0.56}\text{Sb}_{0.44}$ after 10 min exposure to sulfur solution, indicates the reduction of the surface defects.

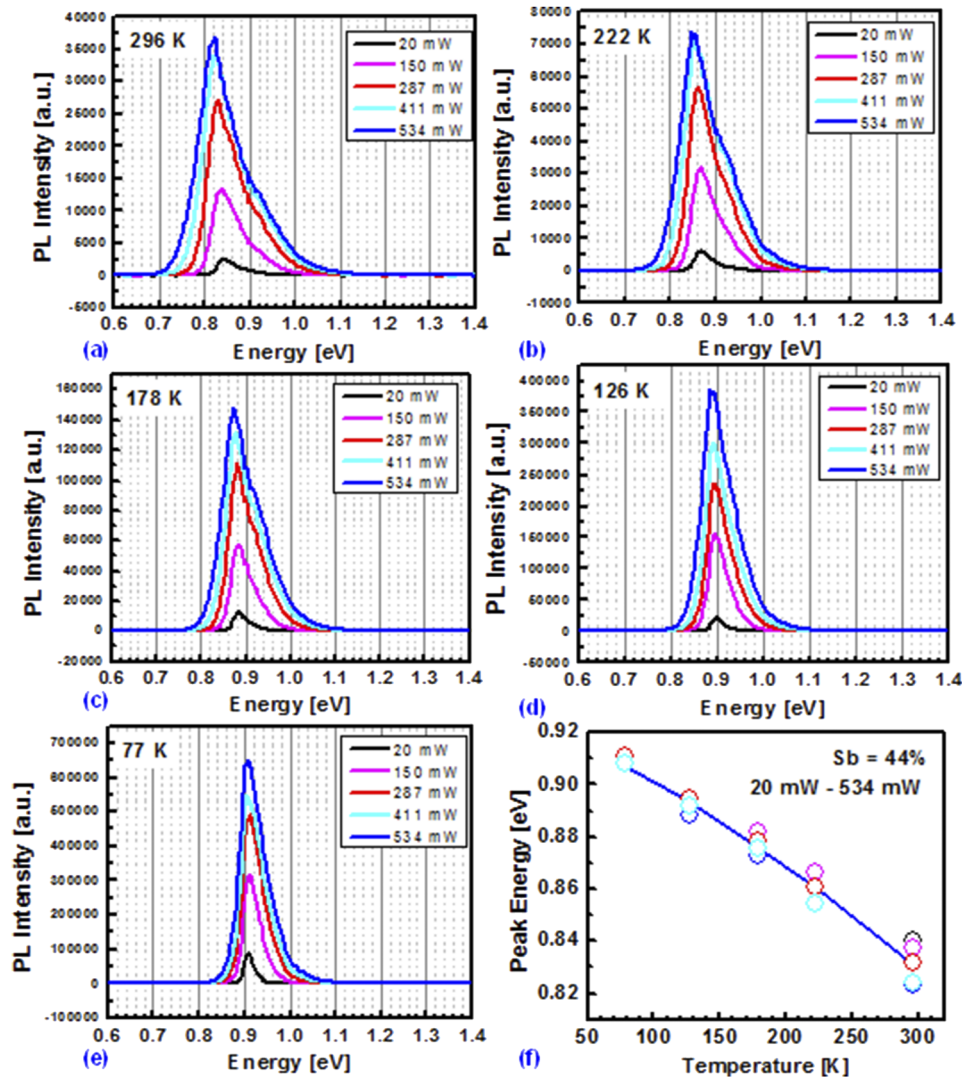


FIG. 7. (a)-(e) Temperature and power dependence PL spectra from $\text{GaAs}_{0.56}\text{Sb}_{0.44}$ sample (Sample-C) after 10 min surface passivation with $(\text{NH}_4)_2\text{S}$ solution. Sample was pre-cleaned with HCl prior to sulfur passivation. (f) PL peak energy versus temperature for $\text{GaAs}_{0.56}\text{Sb}_{0.44}$ sample at laser power in the range of 20 mW to 534 mW and the spot size is 200 μm . The solid line represents the fit to the data using Varshni coefficients, as discussed in the text. Recombination process such as, free-electron to neutral acceptor pairs in $\text{GaAs}_{0.56}\text{Sb}_{0.44}$ after 10 min sulfur passivation as a function of laser power and measurement temperature was identified, leading to a shift in measured recombination energy.

the luminescence spectrum will exhibit a high energy tail characterized by $\exp(-h\nu/kT)$ and a sharp low-energy cut-off at $h\nu = E_g$. This sharp low-energy cut-off is still maintained with decreasing temperature, with the spectrum being more symmetric at any given laser power at 77 K, and the PL line shape becoming sharper while shifting to higher energy at decreased temperatures. The temperature dependence of the bandgap is mainly a consequence of carrier-phonon interactions, wherein at low temperatures, carrier-phonon interactions are greatly reduced, and hence the bandgap is increased. At low laser power excitation and at any measurement temperature from 77 K to 296 K, the PL line shape is asymmetric and it increases with increasing excitation power, due to the large amount of electron-hole pair radiative recombination. Moreover, at 77 K and 534 mW laser power, the spectrum is more symmetric than at 296 K,⁵⁴ which can be explained as follows. At higher temperatures, more carriers are excited which is further away from $k = 0$. As a result, excited carriers are thermalized by the emission of phonons. At lower temperatures, there are less ambient phonons that can be reabsorbed, and also there are less phonons that need to be emitted in order to relax to $k = 0$. The higher

number of excited carriers also means that more phonons would have to be emitted, which can also be reabsorbed by formerly relaxed carriers.

From Figure 7(a)–(e), one can realize that the PL peak energy is shifted to lower energy with increasing the laser power, which the observed trend is the opposite what would be expected for the recombination process due to a DAP recombination process.^{53,55} It is well documented that the DAP recombination peak energy should shift towards lower energy with decreasing excitation intensity and the energy of the recombination is given by^{53,55}

$$E(r) = E_g - (E_A + E_D) + \frac{e^2}{\epsilon r}, \quad (1)$$

where, E_A and E_D are the acceptor and donor binding energies, r is the distance between the pairs, ϵ is the static dielectric constant, and E_g is the band gap energy. The pairs with smaller r will have higher transition probability compared to those with larger r . The closed pairs (smaller r) will decay more rapidly than distant pairs (larger r) due to a higher recombination probability. As a result, increasing the excitation intensity (*i.e.*, laser power) will favor the closer pairs and, according to equation (1), the recombination peak energy $E(r)$ will move towards higher energies. For a direct bandgap semiconductor (*e. g.*, GaAs, InP, InGaAs, *etc*), the DAP peak shift is small and only limited to few meV (~ 3.5 meV for GaP) per tenfold change in excitation intensity.⁵⁵ In Figure 7(a)–(e), the peak energy change is limited to ~ 16 meV, 15 meV, 12 meV, 10 meV, and 0 meV with the laser power ranging from 20 mW to 534 mW at 296 K, 222 K, 178 K, 126 K, and 77 K; respectively, but in the opposite direction. This pattern of the shift in peak's position can confirm that the recombination process is not related to DAP. Therefore, we infer the recombination process is due to free-electrons to neutral acceptors (since the acceptor activation energy was determined to be ~ 50 meV, as shown in Figure 12 below). Since the activation energy of donors in GaAs is limited to be about 6 meV (assume to be the same for GaAs_{0.56}Sb_{0.44}), and the thermal energy is ~ 7 meV at 77 K and hence most of the donors will ionize at this temperature. As a result, the recombination will be due to free-electrons to neutral acceptors. The change in the bandgap energy due to the alteration of the laser power follows the same trend as one would expect for the variation of samples' temperature.⁵³ Unlike the measurements at lower temperatures with the flow of liquid nitrogen, we expect the samples' temperature could increase above room temperature as we increased the laser power. As a result, the PL peak energy position will remain almost constant irrespective of the laser power's variation at lower temperatures, as shown in Figure 7(e). In addition, thermally excited carriers in the high laser power regime (534 mW) at 296 K could be responsible for the asymmetric PL spectrum (Figure 7a) where this asymmetry was not apparent at 77 K (Figure 7e) with the same laser power. This conclusion is supported from the fact that the PL peak energy separation decreased from 16 meV at 296 K to ~ 0 meV at 77 K. Thus, we can conclude that the recombination process is due to the free-electrons to neutral acceptors.

Figure 7(f) shows the experimental PL peak energy as a function of measurement temperature and laser excitation power. The bandgap of the GaAs_{0.56}Sb_{0.44} sample increases with decreasing temperature due to the change in thermal expansion of lattice and bandgap energy renormalization by electron-phonon interaction.^{4,5,56,57} When the temperature increases, the amplitude of atomic vibrations increases, leading to a larger interatomic spacing. As a result, the decrease in potential seen by the electrons in the material reduces the size of the energy bandgap. The temperature dependent experimental values of the bandgap, $E_g(T)$, were simultaneously fit with an empirical relation given by the Varshni equation,

$$E_g(T) = E_g(0) - \frac{\alpha T^2}{\beta + T} \quad (2)$$

where $E_g(0)$ is the bandgap at 0 K, α and β are the Varshni coefficients. The solid line fitted to the experimental results yielded values of $\alpha = 4.8 \times 10^{-4} eV/K$ and $\beta = 189K$, showing an excellent fit to our experimental results. In addition, our results are in agreement with other researchers of the same material.^{4,5,56,57} In fact, these values were found to be independent of the surface orientations where (001), (001)/8° towards (111)B, (001)/8° towards (111)A, and (115)B were used in Ref. 5. One can conclude that the sulfur passivation is needed to remove native oxides and to reduce the surface dangling bonds prior to the deposition of high- κ dielectrics. In the next section, we will

further demonstrate the effectiveness of the sulfur passivation after the Al_2O_3 deposition through photoluminescence spectroscopy.

E. Stability of $(\text{NH}_4)_2\text{S}$ surface passivation on $\text{GaAs}_{0.66}\text{Sb}_{0.34}$ surfaces

In order to investigate the stability of sulfur passivation on the $\text{GaAs}_{0.66}\text{Sb}_{0.34}$ surfaces, which were carried out in one year apart and after the deposition of Al_2O_3 on those surfaces, PL measurements were performed on two samples that were passivated by sulfur and Al_2O_3 layers with the second sample being treated one year after the first. These two samples (*i.e.*, passivated with sulfur and ALD Al_2O_3 layer on top, carried out one year apart) were selected for PL analysis to examine if the sulfur passivation deteriorates over time when capped with an oxide layer. Note that the oxide is transparent for all of the wavelength ranges studied, so it will not interfere with the PL results herein. In addition, no specific steps were taken to preserve these samples. The samples were stored in atmosphere at ambient temperatures. In both cases, the combined HCl and $(\text{NH}_4)_2\text{S}$ passivation scheme was used to passivate the $\text{GaAs}_{0.66}\text{Sb}_{0.34}$ sample prior to the deposition of 4 nm and 10 nm ALD Al_2O_3 layers. The combination of an HCl pre-clean, sulfur passivation and ALD deposited Al_2O_3 were considered as a prescribed solution for the removal of native oxides on GaAs and GaSb samples.^{58,59} In addition, an increased PL emission intensity provides direct evidence of the reduced surface recombination velocity as well as the reduced surface dangling bonds after the sulfur passivation and Al_2O_3 dielectric deposition. Figure 8 shows room temperature PL spectra from the surface of $\text{GaAs}_{0.66}\text{Sb}_{0.34}$ (Sample-B), with the deposition of a 10 nm Al_2O_3 layer and sulfur passivation performed one year apart. PL measurements were performed through the Al_2O_3 layer. The freshly passivated sample (blue) exhibited a 2× increase in PL intensity as compared with the sample that had been passivated one year prior (red). Note that both GaAsSb samples have the same Sb composition and both were cleaned with dilute HCl solution for 10 min prior to the Al_2O_3 deposition. The S atoms replaced the surface position of oxygen atoms that were previously bonded with Ga and Sb atoms, thus preventing the formation of GaO_x and SbO_x native oxides,³⁹ resulting in a higher PL intensity. The unwanted native oxides were eliminated after the 10 min HCl pre-clean, 10 min sulfur passivation and Al_2O_3 layer deposition, as discussed in detail in our recent work using XPS.³⁹ Sulfur atoms bonded with Ga and Sb atoms are well-preserved after Al_2O_3 deposition at 250°C ALD deposition temperature.³⁹ If this was not the case, the luminescence intensity would have been affected after the Al_2O_3 deposition. Moreover, the PL intensity was degraded for the sample that was passivated one year prior, indicating the reduced effectiveness of sulfur bonding with Ga, As and Sb atoms. One can conclude that the GaAsSb surface passivated with sulfur capped with Al_2O_3 will

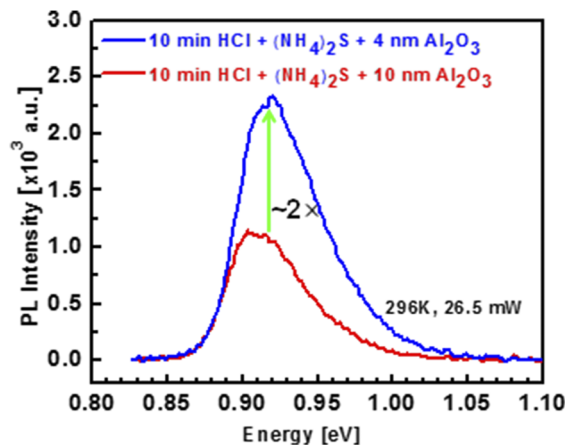


FIG. 8. Room temperature PL spectra from the surface of $\text{GaAs}_{0.66}\text{Sb}_{0.34}$ (Sample-B) with a 4 nm-10 nm Al_2O_3 layer. The intensity of the freshly passivated sample (blue) was approximately 2× that of the sample that had been passivated one year earlier (red). This was due to preventing the formation of GaO_x and SbO_x native oxides by S atom bonded with Ga and Sb atoms. Both GaAsSb samples have the same composition and both were cleaned with dilute HCl solution for 10 min prior to Al_2O_3 deposition.

deteriorate over time and it could be due to the formation of oxides at the heterointerface of dielectric/GaAsSb.

F. Sb composition dependent optical properties via PL spectroscopy

PL spectroscopy was performed on GaAs_{1-y}Sb_y alloys to determine the direct gap as a function of Sb alloy composition. Figures 9(a)–(b) show the PL spectra of the studied GaAs_{1-y}Sb_y alloys at 296 K and 77 K, respectively, with an excitation laser power of 26.5 mW. These spectra were offset and an asymmetric double sigmoidal function was utilized in order to determine the peak position and the FWHM. The sharp low-energy tail of the GaAs_{1-y}Sb_y alloys at 77 K, demonstrated in Figure 9(b), is an indication of the high-quality of these materials. As opposed to the ternary alloys and GaAs, Te-doped GaSb shows two peaks at 77 K, as discussed below. Figure 9(c) shows the bandgap as a function of alloy composition at 296 K and 77 K, and data are tabulated in Table II. The solid lines in Figure 9(c), are fits of the composition dependence of the bandgap to a second order polynomial, with the fit equations being Equation (3) and (4) for 296 K and 77 K, respectively:

$$E_g(296K) = 1.418 - 1.78y + 1.09y^2, \quad (3)$$

$$E_g(77K) = 1.502 - 1.89y + 1.21y^2, \quad (4)$$

where, y is the Sb content in GaAs_{1-y}Sb_y. Other groups have obtained a room temperature bandgap dependence of $E_g(296K) = 1.43 - 1.9y + 1.2y^2$ for GaAsSb alloys grown via metal-organic vapor phase epitaxy (MOVPE) and liquid phase epitaxy^{4,5,7} (dashed line in Figure 9(c)), which is in

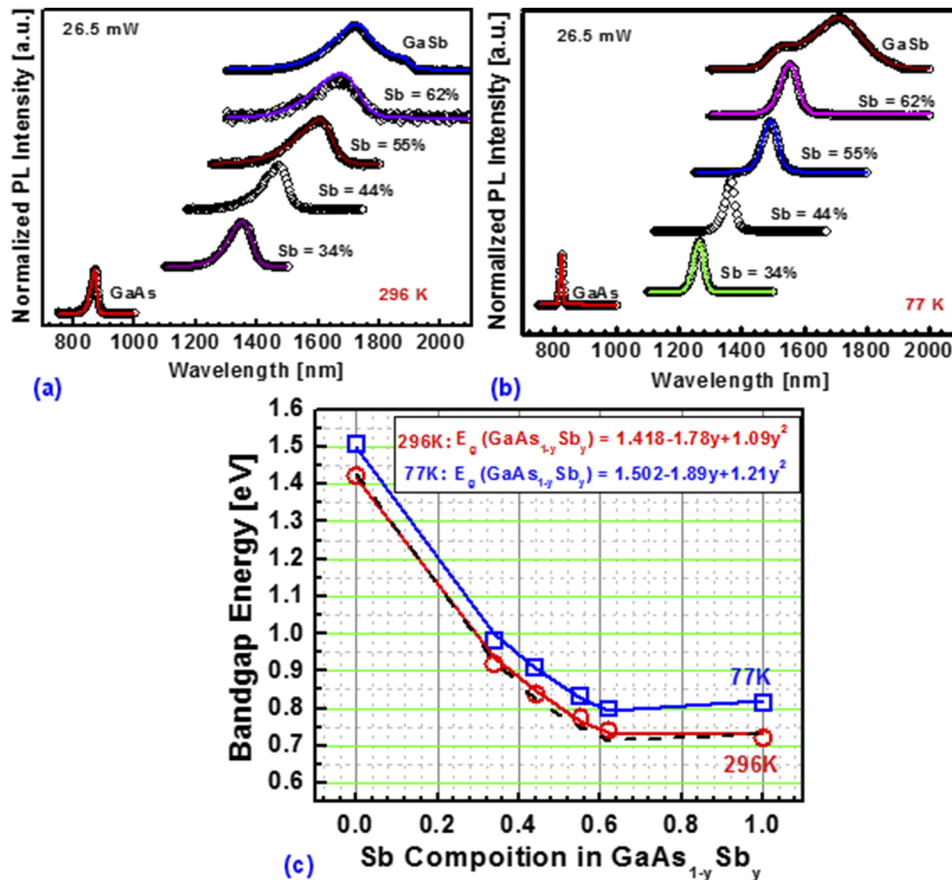


FIG. 9. PL spectra at 296 K (a) and 77 K (b) as a function of Sb composition in GaAs_{1-y}Sb_y obtained using at 26.5 mW laser power. (c) Bandgap energy measured by PL as a function of Sb composition. All the samples were sulfur passivated except for the 44% Sb composition sample. The sharp low-energy tail of the GaAs_{1-y}Sb_y alloys at 77 K is an indication of the high-quality GaAsSb materials.

TABLE II. Bandgaps of Sb composition dependent GaAs_{1-y}Sb_y alloys at 296 K and 77 K determined by PL.

Sb composition (%)	E _g (eV)	
	296 K	77 K
0	1.423	1.506
34	0.918	0.980
44	0.840	0.908
55	0.775	0.833
62	0.742	0.797
100	0.719	0.813

agreement with our calculated fit at 296 K. Note that each of our final Sb composition GaAsSb samples was grown using step-graded buffer so that the defects are minimal in the uppermost layer, as discussed above. The PL results demonstrate the quality of GaAsSb materials over the entire range of Sb composition through the step-graded buffer approach using our MBE growth process.

G. Sb composition and laser power dependent optical properties via PL

Figures 10(a)–(e) show the laser power dependence of the PL of various GaAs_{1-y}Sb_y alloys ($0 \leq y \leq 1$) at 77 K, after passivation with sulfur for 10 min in (NH₄)₂S solution. The PL spectra in Figure 10(a)–(e) were normalized to the luminescence peak intensity, offset, and fit to an asymmetric double sigmoidal function in order to determine the peak position as well as the FWHM. As can be seen in Figures 10(a)–(b), the peaks for GaAs and GaAs_{0.66}Sb_{0.34} demonstrate a red shift in peak energy with increasing excitation intensity. As the intensity of light increases due to the increase in laser power, a variation in the number of excited charge carriers can occur in the conduction and valence band. As a result, the interaction between these charge carriers could be responsible for red shift of the PL emission.^{60,61} At high enough excitation laser power, the lower energy conduction band states can start to become filled effectively, resulting in blue shifting of the PL emission.^{62,63} We note that such a change in emission properties cannot be due to GaAsSb phase decomposition, as phase decomposition would alter the PL peak position due to the creation of different Sb composition-bearing regions inside the GaAsSb epilayer. Thus, the observed shift is similar to the Moss-Burstein effect used to describe the apparent band gap variation as a function of doping in semiconductors. A similar effect can also be observed in the PL emissions of semiconductors, such as in InP⁶¹ and the indirect gap of Ge^{64,65} as a function of the excitation intensity. Therefore, we attribute the blue shift in PL emission of GaAs_{0.38}Sb_{0.62} to a Moss-Burstein-like shift. As the Moss-Burstein shift and band gap renormalization are competing effects, the lack of a spectral shift in GaAs_{0.45}Sb_{0.55} could be the consequence of the partial cancellation of these effects.

In order to determine the origins of the PL emissions, the integrated PL intensity (IPL) as a function of excitation intensity was examined (Figure 11). IPL can be fit to $I = CP^k$, with I being the IPL, C a proportionality constant, power P , and k is an exponent related to the different recombination mechanisms.^{53,66} The value of k is representative of the mechanism, with $1 \leq k \leq 2$ typically attributed to interband transitions, while $k < 1$ is indicative of a DAP recombination or free-to-bound (FB) transition.^{53,66,67} Since we have varied only 4 laser power (25 mW to 249 mW) during this measurement, the value of k might differ depends on the data set used during fitting of the line. However, we can find that the value of k is in the range of 0.8 to 1.2, so the recombination process could be due to free-electrons to neutral acceptors or Sb-related-defects states since the thermal energy is approximately 7 meV at 77 K. In order to quantify their associated activation energy, the temperature dependent integrated intensity of PL data (I_T) (Figure 7a–e) can be fitted with the following equation^{68–72} especially in the 200 K–296 K experimental data range:

$$I_T = \frac{I_0}{1 + \alpha \exp(-E_A/kT)}, \quad (5)$$

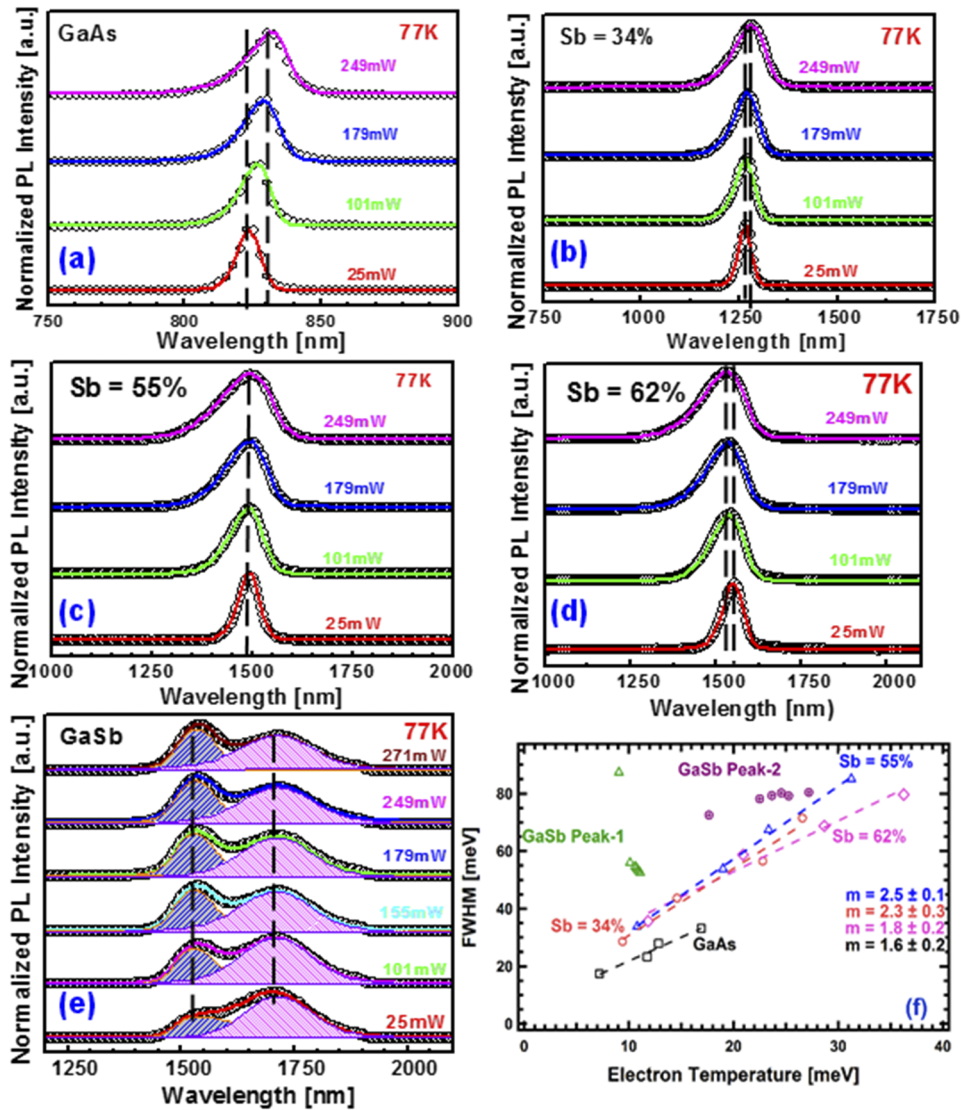


FIG. 10. (a)-(e) Power dependence PL spectra from various $\text{GaAs}_{1-y}\text{Sb}_y$ samples measured at 77 K. The peak positions of each sample were shifted vertically to observe the peak development as a function of excitation power in $\text{GaAs}_{1-y}\text{Sb}_y$ materials. (f) FWHM as a function of the electron temperature at 77 K (m is the slope). The different recombination processes in Sb composition dependent $\text{GaAs}_{1-y}\text{Sb}_y$ materials, as a function of laser power and measurement temperatures, indicate a successful transfer of the mixed As-Sb buffer growth on Si (Sb=0.55).

where, α is the recombination process rate parameter, I_0 is the proportionality constant, and E_A is activation energy. The fitted data (show by green color in each laser power) in Figure 12 yields activation energy in the range of 52 meV-62 meV in the power range studied in this work. Since our GaAsSb epitaxial layers were p -type, as determined by metal-oxide-semiconductor capacitor results, we assign this impurity level is neutral acceptors or Sb-related-defects states located within the bandgap of $\text{GaAs}_{0.56}\text{Sb}_{0.44}$ material. Based on impurity levels within the GaSb⁷³ and GaAs⁷⁴ materials, we can qualitatively conclude that the main PL peak is due to the Sb-related recombination process, *e.g.*, Sb anti-site defects or vacancies. We thus conclude that the origin of the peaks for GaAs and $\text{GaAs}_{0.38}\text{Sb}_{0.62}$ (and $\text{GaAs}_{0.45}\text{Sb}_{0.55}$) arise from excitonic or band-to-band (BB) transitions and free-electrons to neutral acceptor recombination or Sb-related-defects states, respectively.

Figure 10(f) shows the dependence of the FWHM as a function of the electron temperature. For BB transitions, the high-energy tail of PL should follow a Fermi-Dirac distribution, which was used in order to determine the electron temperature (since GaAsSb materials are p -type) at each

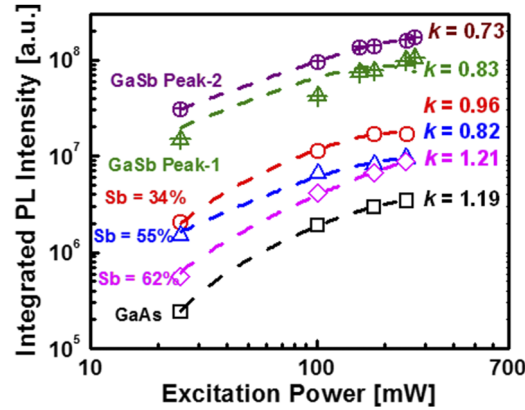


FIG. 11. Integrated PL intensity as a function of laser power for various Sb contents. The integrated PL intensity as a function of laser excitation power indicates the excitonic transition from 34% and 62% GaAsSb epitaxial layers.

excitation power. From Figure 10(f), it can be seen that the FWHM is linear with the electron temperature for ternary alloys, with the slopes, m , for $\text{GaAs}_{0.66}\text{Sb}_{0.34}$ and $\text{GaAs}_{0.45}\text{Sb}_{0.55}$ being greater than that for GaAs and $\text{GaAs}_{0.38}\text{Sb}_{0.62}$. For a BB transition, assuming that the Fermi-Dirac distribution can be approximated as a Maxwell-Boltzmann distribution, the slope of the FWHM as a function of the electron temperature should be $1.8kT$ ⁷⁵ where k is the Boltzmann constant and T is the electron temperature. In our case, at the highest excitation intensities, the deviation of kT obtained by the Fermi Dirac distribution and Maxwell Boltzmann distribution is less than 2 meV. For a DAP recombination, increasing the excitation density can lead to a filling of the donor or acceptor states, and the energy of the transition depends on the separation distance between the donor and acceptor states. As the excitation intensity increases, more donors and acceptors will trap an electron and a hole, respectively, decreasing the average distance of the donors and acceptors involved in this transition, causing a blue shift in the emission frequency.⁵³ However, this shift will eventually vanish as the distance between the donors and acceptors reaches the minimum separation. Thus we cannot necessarily distinguish the difference between a DAP and FB recombination using this method.

Figure 10(e) shows the 77 K PL spectra from the Te-doped GaSb bulk sample (Wafer Technology, UK). One can observe two PL transitions, i) one located at 0.807 eV (peak-1: 1537 nm) and ii) one located at 0.725 eV (peak-2: 1710 nm). It is well documented that undoped GaSb is *p*-type due to native acceptor impurities that are related to Sb deficiencies,⁷⁶ Ga vacancies (V_{Ga}), Ga on Sb sites (Ga_{Sb}) and $\text{Ga}_{\text{Sb}}V_{\text{Ga}}$ complexes. The Te-dopant is incorporated within the undoped GaSb, which was

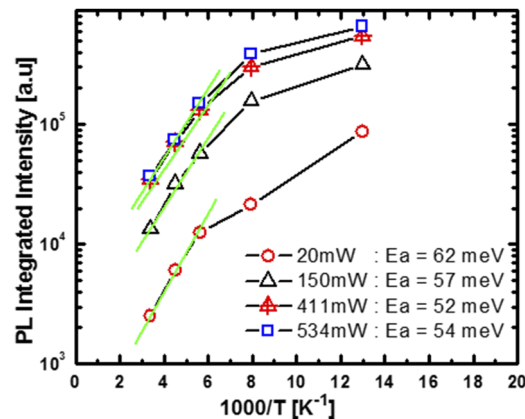


FIG. 12. Integrated PL intensity as a function of measurement temperature. The fitted integrated PL intensity in the temperature range of 200 K-296 K indicates the activation energy in the range of 52 meV to 62 meV depending on the laser power used during measurement.

p-type, in order to reduce the net carrier concentration and thus achieve high resistivity. Te-doped GaSb was previously explored in detail,^{73,76,77} including at 77 K where a DAP or FB transition was the dominant transition, with contributions to the lower energy side arising from a double electron capture in the double acceptor $V_{Ga}Ga_{Sb}$, making it appear as if there was a single peak, and depending on the Te concentration, a weak BB transition was observed.⁷⁸ Following these designations, we attribute the lower energy peak (0.725 eV) to a DAP or FB transition, and the higher energy peak (0.807 eV) to be related to the BB or excitonic recombination. The FB or DAP recombination in Ref. 78 involves an acceptor state that is around 82 meV deep at 2 K, which matches closely to the separation of our peak positions. While the IPL of the lower energy peak matches the attribution given by Ref. 78, the IPL of the higher energy peak and the electron temperature dependence of the FWHM suggests that this transition is a result of FB or DAP. In order to explain this, the deconvolution of the GaSb fits is shown in Figure 10(e). At an excitation intensity of 25 mW, the low energy (high wavelength) tail of the high energy peak is very broad, and narrows substantially with a 101 mW excitation and is accompanied by a significant lowering of the FWHM. The broad low-energy tail can be attributed to recombination involving defect states, which saturate as the excitation intensity increases. As these defect states saturate, the relative intensity of the BB transitions will increase and becoming increasingly more dominant, leading to a decrease in the FWHM. As this peak involves defect states, the integrated PL can be expected to deviate from the behavior of excitonic or BB transition. Furthermore, the increase in relative peak intensity of the higher energy peak to that of the lower energy peak can be attributed to saturation of the donors and acceptors with high excitation intensity.^{79–81}

IV. CONCLUSION

The impact of bulk and surface defect states on the vibrational and optical properties of step-graded $GaAs_{1-y}Sb_y$ ($0 \leq y \leq 1$) materials with and without chemical surface treatment via sulfur passivation was investigated. Tunable Sb composition $GaAs_{1-y}Sb_y$ epitaxial layers were realized using an optimized growth process taking into consideration the growth temperature, Sb/Ga flux ratio, and Sb/As flux ratio as functions of Sb composition. Utilizing this materials synthesis procedure, low bulk defect $GaAs_{1-y}Sb_y$ materials were heterogeneously integrated on GaAs and Si substrates. Raman spectroscopy results demonstrated consistent FWHM values across the entire Sb composition range, indicating that increasing Sb compositions can be achieved without the introduction of additional bulk defects that might otherwise degrade the $GaAs_{1-y}Sb_y$ crystallinity. Moreover, PL analysis of as-grown and $(NH_4)_2S$ -treated $GaAs_{1-y}Sb_y$ epitaxial layers revealed a reduction in surface defect states following $(NH_4)_2S$ treatment as observed *via* a $1.3\times$ enhancement in PL intensity. Using a wide range of measurement temperatures (varying from 77 K to 296 K) and excitation intensities (20 mW to 534 mW), we have established a relationship between Sb composition and optical emissions as well as quantified the luminescence mechanisms pertaining to $GaAs_{1-y}Sb_y$ materials. Through the later, and in comparison with binary GaAs and GaSb, it was found that free-to-bound recombination related to Sb anti-site defects or vacancies are responsible for recombination while analyzing optical properties in $GaAs_{1-y}Sb_y$ epitaxial layers. Additionally, PL analysis demonstrated the short- and long-term thermodynamic stability of the $GaAs_{1-y}Sb_y/Al_2O_3$ heterointerface, revealing an absence of quantifiable atomic interdiffusion and the suppression of native oxide formation during Al_2O_3 ALD. In summary, the presented results provide a comprehensive means of quantifying the impact of bulk and surface defects on mixed As-Sb optical properties, thereby providing a pathway towards the realization of $GaAs_{1-y}Sb_y$ optoelectronic devices.

ACKNOWLEDGMENTS

M. C. and J.-S. L. acknowledge partial support from the NSF under grant number ECCS-1507950. Authors would like to acknowledge Patrick Goley for assistance with TEM imaging. Lastly, the authors acknowledge the NCFL-Institute for Critical Technology and Applied Science, Virginia Tech Nanofabrication facilities, and Charles Farley for assistance in materials characterization. G. K. and M. M. acknowledge the support of the AFOSR through grant FA9550-14-1-0376 and DURIP2016 through grant FA9550-16-1-0358. We also thank the support from Virginia Tech's Open Access Subvention Fund.

- ¹ X. Sun, S. Wang, J. S. Hsu, R. Sidhu, X. G. Zheng, X. Li, J. C. Campbell, and A. L. Holmes, Jr., *IEEE J. Sel. Top. Quantum Electron.* **8**, 817 (2002).
- ² Y. Zhu and M. K. Hudait, *Nanotechnol. Rev.* **2**, 637 (2013).
- ³ M. Yano, M. Ashida, A. Kawaguchi, Y. Iwai, and M. Inoue, *J. Vac. Sci. Technol. B* **7**, 199 (1989).
- ⁴ D. Huang, J. Chyi, J. Klem, and H. Morkoc, *J. Appl. Phys.* **63**, 5859 (1988).
- ⁵ R. Lukic-Zrnica, B. P. Gorman, R. J. Cottier, T. D. Golding, C. L. Littler, and A. G. Norman, *J. Appl. Phys.* **92**, 6939 (2002).
- ⁶ T. C. McGlenn, T. N. Krabach, M. V. Klein, G. Bajor, J. E. Greene, B. Kramer, S. A. Barnett, A. Lastras, and S. Gorbatskin, *Phys. Rev. B* **33**, 8396 (1986).
- ⁷ R. M. Cohen, M. J. Cherng, R. E. Benner, and G. B. Stringfellow, *J. Appl. Phys.* **57**, 4817 (1985).
- ⁸ E. Papis-Polakowska, *Electron Technology-Internet Journal* **38B**, 1 (2005/2006).
- ⁹ M. Fuzimatsu, H. Saito, and Y. Miyamoto, *IEEE Electron Device Meeting* 2013, pp. 25–28.
- ¹⁰ D. Serries, M. Peter, N. Herres, K. Winkler, and J. Wagner, *J. Appl. Phys.* **87**, 8522 (2000).
- ¹¹ H. Kroemer, *Physica E* **20**, 196 (2004).
- ¹² J.-S. Liu, Y. Zhu, P. S. Goley, and M. K. Hudait, *ACS Appl. Mater. Interfaces* **7**, 2512 (2015).
- ¹³ B. Rajamohanan, D. Mohata, D. Zhernokletov, B. Brennan, R. M. Wallace, R. Engel-Herbert, and S. Datta, *Appl. Phys. Express* **6**, 101201 (2013).
- ¹⁴ D. Mohata, B. Rajamohanan, T. Mayer, M. K. Hudait, J. Fastenau, D. Lubyshev, A. W. K. Liu, and S. Datta, *IEEE Electron Device Lett.* **33**, 1568 (2012).
- ¹⁵ Y. Zhu, M. K. Hudait, D. K. Mohata, B. Rajamohanan, S. Datta, D. Lubyshev, J. M. Fastenau, and A. K. Liu, *J. Vac. Sci. Technol. B* **31**, 041203 (2013).
- ¹⁶ Y. Zhu, N. Jain, S. Vijayaraghavan, D. Mohata, S. Datta, D. Lubyshev, J. M. Fastenau, A. K. Liu, and M. K. Hudait, *J. Appl. Phys.* **112**, 094312 (2012).
- ¹⁷ Y. Zhu, D. K. Mohata, S. Datta, and M. K. Hudait, *IEEE Trans. Device and Materials Reliability* **14**, 245 (2014).
- ¹⁸ B. Rajamohanan, D. Mohata, Y. Zhu, M. K. Hudait, Z. Jiang, M. Hollander, G. Klimeck, and S. Datta, *J. Appl. Phys.* **115**, 044502 (2014).
- ¹⁹ S. S. Yi, S. J. Chung, H. Rohdin, M. H. D. Bour, N. Moll, D. R. Chamberlin, and J. Amano, *International Conf. Indium Phosphide and Related Materials*, 2003, pp. 380–384.
- ²⁰ B. T. McDermott, E. R. Gertner, S. Pittman, C. W. Seabury, and M. F. Chang, *53rd Annual Device Research Conference Digest*, Charlottesville, VA, USA, 1995, pp. 90–91.
- ²¹ M. W. Dvorak, C. R. Bolognesi, O. J. Pitts, and S. P. Watkins, *IEEE Electron Dev. Lett.* **22**, 361 (2001).
- ²² S. W. Cho, J. H. Yun, D. H. Jun, J. I. Song, I. Adesida, N. Pan, and J. H. Jang, *Solid-State Electron.* **50**, 902 (2006).
- ²³ X. Sun, J. Hsu, X. G. Zheng, J. C. Campbell, and A. L. Holmes, Jr., *IEEE Photon. Technol. Lett.* **14**, 681 (2002).
- ²⁴ X. Sun, S. Wang, X. G. Zheng, X. Li, J. C. Campbell, and A. L. Holmes, Jr., *J. Appl. Phys.* **93**, 774 (2003).
- ²⁵ Y. Eguchi, M. Shiokawa, K. Sakamoto, and K. Yamaguchi, *IEEE Photovoltaic Spec. Conf.* (2012), 45.
- ²⁶ Y. Kim, K.-Y. Ban, C. Zhang, and C. B. Honsberg, *Appl. Phys. Lett.* **107**, 153103 (2015).
- ²⁷ J. F. Klem, O. Blum, S. R. Kurtz, I. J. Fritz, and K. D. Choquette, *J. Vac. Sci. Technol. B* **18**, 1605 (2000).
- ²⁸ T. Anan, M. Yamada, K. Nishi, K. Kurihara, K. Tokutome, A. Kamei, and S. Sugou, *Electron. Lett.* **37**, 566 (2001).
- ²⁹ O. Blum and J. F. Klem, *IEEE Photonics Technol. Lett.* **12**, 771 (2002).
- ³⁰ W. Qiu, X. Wang, P. Chen, N. Li, and W. Lu, *Appl. Phys. Lett.* **105**, 082104 (2014).
- ³¹ M. K. Hudait, Y. Zhu, P. Goley, M. Clavel, and N. Jain, *Appl. Phys. Express* **8**, 025501 (2015).
- ³² H. S. Kim, Y. K. Noh, M. D. Kim, Y. J. Kwon, J. E. Oh, Y. H. Kim, J. Y. Lee, S. G. Kim, and K. S. Chung, *J. Cryst. Growth* **301-302**, 230 (2007).
- ³³ W. Lee, S. Kim, S. Choi, H. Lee, S. Lee, S. Park, T. Yao, J. Song, H. Ko, and J. Chang, *J. Cryst. Growth* **305**, 40 (2007).
- ³⁴ Y. K. Noh, Y. J. Hwang, M. D. Kim, Y. J. Kwon, J. E. Oh, Y. H. Kim, and J. Y. Lee, *J. Korean Phys. Soc.* **57**, 173 (2010).
- ³⁵ E. Papis, A. Piotrow, E. Kaminska, K. Golaszewska, R. Kruska, T. T. Piotrowski, W. Rzedkiewicz, J. Szade, A. Winiarski, and A. Wawro, *Phys. Stat. Sol. (c)* **4**, 1448 (2007).
- ³⁶ Y. Wu, D. Fang, L. Xu, X. Ma, J. Tang, X. Gao, R. Li, S. Niu, and X. Wang, *International Conference on Optoelectronics and Microelectronics (ICOM)*, 2015, pp. 411–414.
- ³⁷ N. An, G. Liu, Z. Wei, R. Deng, X. Fang, X. Gao, Y. Zhou, M. Li, and X. Ma, *International Conference on Optoelectronics and Microelectronics (ICOM)*, 2012, pp. 25–29.
- ³⁸ M.-L. Tsai, J.-Y. Ko, S.-Y. Wang, and C.-H. Chien, *IEEE Trans. Electron. Dev.* **63**, 3459 (2016).
- ³⁹ J.-S. Liu, M. B. Clavel, and M. K. Hudait, *ACS Applied Materials & Interfaces* **7**, 28624 (2015).
- ⁴⁰ G. P. Schwartz, *Thin Solid Films* **103**, 3 (1983).
- ⁴¹ P. T. Chen, Y. Sun, E. Kim, P. C. McIntyre, W. Tsai, M. Garner, P. Pianetta, Y. Nishi, and C. O. Chui, *J. Appl. Phys.* **103**, 034106 (2008).
- ⁴² S. McDonnell, D. M. Zhernokletov, A. P. Kirk, J. Kim, and R. M. Wallace, *Appl. Surf. Sci.* **257**, 8747 (2011).
- ⁴³ D. Misra, *ECS Trans.* **41**, 109 (2011).
- ⁴⁴ A. Ali, H. S. Madan, A. P. Kirk, D. A. Zhao, D. A. Mourey, M. K. Hudait, R. M. Wallace, T. N. Jackson, B. R. Bennett, J. B. Boos, and S. Datta, *Appl. Phys. Lett.* **97**, 143502 (2010).
- ⁴⁵ V. M. Bermudez, *J. Appl. Phys.* **114**, 024903 (2013).
- ⁴⁶ M. Barth, G. B. Rayner, Jr., S. McDonnell, R. M. Wallace, B. R. Bennett, R. Engel-Herbert, and S. Datta, *Appl. Phys. Lett.* **105**, 222103 (2014).
- ⁴⁷ A. Nainani, T. Irisawa, Z. Yuan, B. R. Bennett, J. B. Boos, Y. Nishi, and K. C. Saraswat, *IEEE Trans. Electron Devices* **58**, 3407 (2011).
- ⁴⁸ I. Geppert, M. Eizenberg, A. Ali, and S. Datta, *Appl. Phys. Lett.* **97**, 162109 (2010).
- ⁴⁹ Y. Zhu, M. Clavel, P. Goley, and M. K. Hudait, *J. Appl. Phys.* **116**, 134304 (2014).
- ⁵⁰ P. K. Kasanaboina, S. K. Ojha, S. U. Sami, C. L. Reynolds, Jr., Y. Liu, and S. Iyer, *Semicond. Sci. Technol.* **30**, 1 (2015).
- ⁵¹ J. Robertson, Y. Guo, and L. Lin, *J. Appl. Phys.* **117**, 112806 (2015).

- ⁵² M. V. Lebedev, E. V. Kunitsyna, W. Calvet, T. Mayer, and W. Jaegermann, *J. Phys. Chem. C* **117**, 15996 (2013).
- ⁵³ V. Swaminathan and A. T. Macrander, *Materials Aspects of GaAs and InP Based Structures* (Prentice Hall, Englewood Cliffs, New Jersey, 1991).
- ⁵⁴ T. R. Merritt, M. A. Meeker, B. A. Magill, G. A. Khodaparast, S. McGill, J. G. Tischler, S. G. Choi, and C. J. Palmström, *J. of Appl. Phys.* **115**, 193503 (2014).
- ⁵⁵ R. Dingle, *Phys. Rev.* **184**, 788 (1969).
- ⁵⁶ K. G. Merkel, V. M. Bright, M. A. Marciniak, C. L. A. Cerny, and M. O. Manasreh, *Appl. Phys. Lett.* **65**, 2442 (1994).
- ⁵⁷ E. T. R. Chidley, S. K. Haywood, A. B. Henriques, N. J. Mason, R. J. Nicholas, and P. J. Walker, *Semicond. Sci. Technol.* **6**, 45 (1991).
- ⁵⁸ C. L. Hinkle, A. M. Sonnet, E. M. Vogel, S. McDonnell, G. J. Hughes, M. Milojevic, B. Lee, F. S. Aguirre-Tostado, K. J. Choi, H. C. Kim, J. Kim, and R. M. Wallace, *Appl. Phys. Lett.* **92**, 071901 (2008).
- ⁵⁹ D. M. Zhernokletov, H. Dong, B. Brennan, M. Yakimov, V. Tokranov, S. Oktyabrsky, J. Kim, and R. M. Wallace, *Appl. Phys. Lett.* **102**, 131602 (2013).
- ⁶⁰ H. Kalt and M. Rinkler, *Phys. Rev. B* **45**, 1139 (1992) and references therein.
- ⁶¹ E. Göbel, H. J. Queisser, and M. H. Pilkuhn, *Solid. Stat. Comm.* **9**, 429 (1971).
- ⁶² E. Burstein, *Phys. Rev.* **93**, 632 (1954).
- ⁶³ T. S. Moss, *Proc. Phys. Soc. B* **67**, 775 (1954).
- ⁶⁴ H. M. van Driel, A. Elci, J. S. Bessey, and M. O. Scully, *Solid Stat. Comm.* **20**, 837 (1976).
- ⁶⁵ R. R. Lieten, K. Bustillo, T. Smets, E. Simoen, J. W. Ager III, E. E. Haller, and J.-P. Locquet, *Phys. Rev. B* **86**, 035204 (2012).
- ⁶⁶ T. Schmidt and K. Lischka, *Phys. Rev. B* **45**, 8989 (1992).
- ⁶⁷ Q. Yu, H. He, L. Gan, and Z. Ye, *RSC Adv.* **5**, 80526 (2015).
- ⁶⁸ B. D. Rezgui, J. Veirman, S. Dubois, and O. Palais, *Phys. Status Solidi A* **209**, 1917 (2012).
- ⁶⁹ J. I. Pankove, *Optical Processes in Semiconductors* (Dover, New York, 1975), p. 160.
- ⁷⁰ J. Krustok, H. Collan, and K. Hjelt, *J. Appl. Phys.* **81**, 1442 (1997).
- ⁷¹ K. Tanaka, Y. Miyamoto, H. Uchiki, K. Nakazawa, and H. Araki, *Phys. Status Solidi A* **203**, 2891 (2006).
- ⁷² D. Bimberg, M. Sondergeld, and E. Grobe, *Phys. Rev. B* **4**, 3451 (1971).
- ⁷³ P. S. Dutta, H. L. Bhat, and V. Kumar, *J. Appl. Phys.* **81**, 5821 (1997).
- ⁷⁴ <http://www.ioffe.ru/SVA/NSM/Semicond/GaAs/bandstr.html>.
- ⁷⁵ M. Grundmann, *The Physics of Semiconductors* (Springer, 2006).
- ⁷⁶ L. Tirado-Mejía, J. A. Villada, M. de los Ríos, J. A. Peñafiel, G. Fonthal, D. G. Espinosa-Arbeláez, H. Ariza-Calderón, and M. E. Rodríguez-García, *Physica B* **403**, 4027 (2008).
- ⁷⁷ S. Iyer, L. Small, S. M. Hegde, K. K. Bajaj, and A. Abul-Fadl, *J. Appl. Phys.* **77**, 5902 (1995).
- ⁷⁸ A. Bignazzi, A. Bosacchi, and R. Magnanini, *J. Appl. Phys.* **81**, 7540 (1997).
- ⁷⁹ J. H. Park, T. K. Lee, Y. K. Noh, M. D. Kim, and E. Oh, *J. Appl. Phys.* **105**, 043516 (2009).
- ⁸⁰ B. Hu, A. Yin, G. Karczewski, H. Luo, S. W. Short, N. Samarth, M. Dobrowolska, and J. K. Furdyna, *J. Appl. Phys.* **74**, 4153 (1993).
- ⁸¹ E. Oh, H. Park, and Y. Park, *Appl. Phys. Lett.* **72**, 70 (1998).